# Reinforcement of Polyether Polyurethane with Dopamine-Modified Clay: The Role of Interfacial Hydrogen Bonding

8 AUTHORS, INCLUDING:

Liping Yang
Institute of Chemical and Engineering Sciences
42 PUBLICATIONS 967 CITATIONS

SEE PROFILE

Shu Huang
KTH Royal Institute of Technology
32 PUBLICATIONS 805 CITATIONS

SEE PROFILE

# Reinforcement of Polyether Polyurethane with Dopamine-Modified Clay: The Role of Interfacial Hydrogen Bonding

Si Lei Phua,[†] Liping Yang,[†] Cher Ling Toh,[†] Shu Huang,[†] Zviad Tsakadze,[†] Soo Khim Lau,[‡] Yiu-Wing Mai,[§] and Xuehong Lu*,[†]

[†]School of Materials Science and Engineering, Nanyang Technological University, 50 Nanyang Avenue, Singapore 639798
[‡]Singapore Institute of Manufacturing Technology, 71 Nanyang Drive, Singapore 638075
[§]School of Aerospace, Mechanical and Mechatronic Engineering, The University of Sydney, NSW 2006 Australia

Ⓢ *Supporting Information*

**ABSTRACT:** Dopamine-modified clay (D-clay) was successfully dispersed into polyether polyurethane (PU) by solvent blending. It is found that the incorporation of D-clay into PU gives rise to significant improvements in mechanical properties, including initial modulus, tensile strength, and ultimate elongation, at a very low clay loading. The large reinforcement could be attributed to the hydrogen bonds between the hard segments of PU and stiff D-clay layers that lead to more effective interfacial stress transfer between the polymer and D-clay. Besides, the interactions between D-clay and PU are also stronger than those between Cloisite 30B organoclay and the PU chains. Consequently, at a similar clay loading, the PU/D-clay nanocomposite has much higher storage modulus than the PU/organoclay nanocomposite at elevated temperatures.



**KEYWORDS:** polydopamine, clay, polyurethane, hydrogen bonds, interface
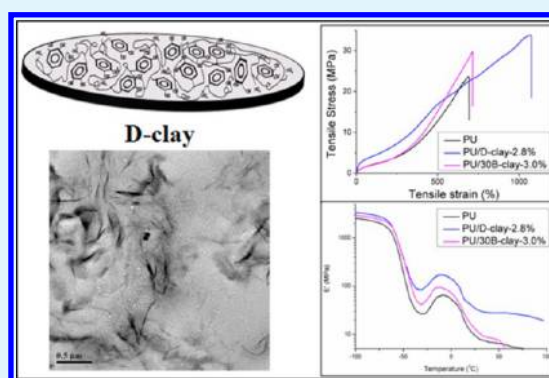
## ■ INTRODUCTION

Polymer nanocomposites have been widely explored in the last two decades. Layered silicates, such as montmorillonite (MMT) clay, are popular candidates for nanoreinforcement, owing to their abundance, low price, and high stiffness.[1] It is commonly accepted that achieving optimum stiffness for nanocomposites will usually require excellent dispersion of the clay. The extent of stiffness enhancements brought by the good clay dispersion, however, varies widely from system to system, for which variation in interfacial interactions is believed to play an important role.

Recent studies have shown that the versatile adhesion of mussel adhesive proteins to various types of material surfaces is related to a high concentration of dopamine units, which are rich in catechol groups, at the interfaces.[2−4] It has been reported that synthetic dopamine is able to self-polymerize on various surfaces under basic conditions to produce adhesive polydopamine (PDA) coatings.[5−8] The PDA coatings can adhere to inorganic surfaces such as metal oxide and silica surfaces by forming coordination chelate bonds, and three to four such bonds can be as strong as a covalent bond.[4] Further, the catechol groups can also form hydrogen bonds with the functional groups of organic polymers,[4] serving as an effective stress transfer agent at the organic−inorganic interfaces. The effective load transfer ability of such interfacial hydrogen bonds has been proven by Messersmith et al.; they successfully incorporated the catechol groups into polyethylene glycol

(PEG), and the modified PEG was bound to clay nanosheets using the layer-by-layer (LbL) deposition technique, leading to great enhancements in both stiffness and toughness of the multilayer thin films.[9] Although LbL assembly is an effective way to realize effective load transfer from polymer matrixes to inorganic nanosheets,[1,10,11] a more generic approach is preferred for large-scale preparation of bulk nanocomposite materials.

Polymer chains of thermoplastic polyurethanes (TPUs) consist of alternating hard and soft segments that may lead to two-phase morphologies due to their thermodynamic incompatibility. The stiffness of TPUs increases with the content of hard microdomains, whereas their elasticity increases with that of soft microdomains. A problem with TPUs is that they usually exhibit low initial moduli and stresses at low to intermediate strains,[12,13] and it is difficult to increase the elastic modulus of a TPU while maintaining its high elasticity and vice versa. TPU/clay nanocomposites have received great attention in the past decade due to their significantly improved mechanical, thermal, and gas barrier properties over those of neat TPUs.[14−20] The enhancements in modulus and elasticity of TPU/clay nanocomposites can be attributed to the dispersion of exfoliated clay layers in the TPUs and the
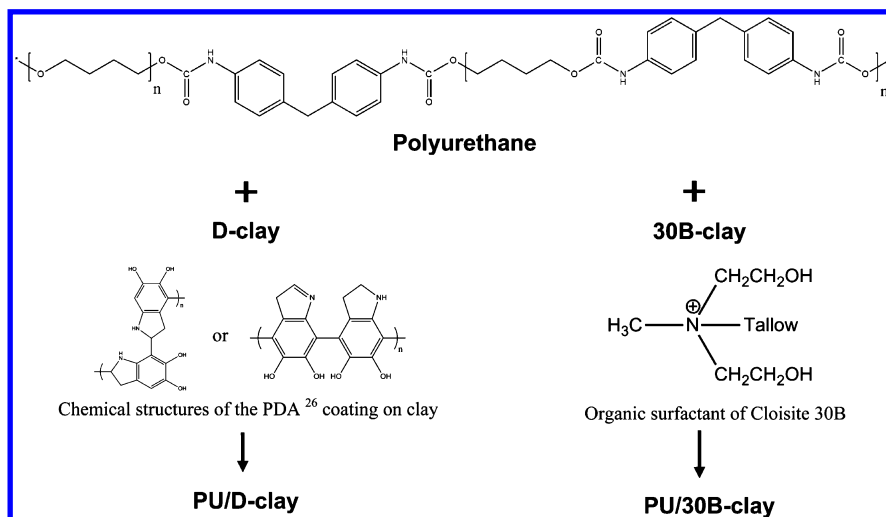
**Scheme 1. Schematic Showing the Chemical Structures of the Constituents in the Nanocomposites**



hydrogen bonding between polyurethane (PU) chains and hydroxylated surfactants attached to clay.[21−23] Obviously, to further enhance the mechanical properties of TPUs, it is essential to create a stronger interface.

Herein, we present a simple approach to prepare high-performance polymer nanocomposites using dopamine-modified clay (D-clay). A polyether-based TPU system was chosen as the matrix since the mechanical properties of TPU are highly dependent on hydrogen bonding. Our results show that significant improvements in mechanical properties, including initial modulus, tensile strength, and ultimate elongation, are achieved at a very low clay loading. The focus of this work is to obtain a better understanding of and insight into the underlying mechanisms for the strong reinforcement effects observed. To eliminate the possibility of forming any interfacial covalent bonds, the TPU/D-clay nanocomposites were prepared through solvent blending and the test samples were fabricated by casting without any high-temperature treatment. This allowed us to reveal the pivotal role played by the hydrogen bonding interactions between D-clay and the PU chains in reinforcing the TPU.

## ■ EXPERIMENTAL SECTION

**Materials.** Polyether-based TPU (Skythane R185A, $M_w$ = 250 000, Shore hardness = 87A, specific gravity = 1.1 g/cm³) was obtained from SK Chemicals (Suwon, Korea). Hard segment of this TPU is made of 4,4′-diphenylmethane diisocyanate and 1,4-butanediol while the soft segment is poly(tetramethylene oxide) glycol ($M_w$ = 1000). Untreated PGW grade sodium MMT (specific gravity = 2.6 g/cm³) with cationic exchange capacity (CEC) of 145 mmol/100 g was obtained from Nanocor, Inc. (Arlington Heights, USA). Tris(hydroxymethyl)-aminomethane (TRIS, 99%) and dopamine hydrochloride (DOPA-HCl, 98%) were purchased from Sigma-Aldrich (Singapore). Acetone (Technical grade, Aik Moh) and dimethylformamide (DMF, HPLC grade, Tedia) were used as-received. To make a fair comparison, Cloisite 30B (30B-clay, specific gravity of Cloisite Na⁺ = 2.86 g/cm³, CEC of Cloisite Na⁺ = 92 mmol/100 g) was chosen as reference material since it is the most popular commercially available organoclay for the TPU system.[19] Cloisite 30B was supplied by Southern Clay Products (Gonzales, TX), and it was dried in a vacuum oven at 80 °C for 24 h before use.

**Preparation of D-Clay and Its Nanocomposites.** D-clay was synthesized using the method reported in our earlier publication.[24] PU/D-clay nanocomposites were prepared through solution mixing. Five grams of PU was first dissolved in 50 mL of DMF by magnetic

stirring for 24 h. A certain amount of D-clay in DMF was then added into the PU solution and stirred continuously for 24 h. PU films were obtained by casting the viscous solution onto glass slides and subsequently removing the solvent at 60 °C in vacuum for 24 h. The reference material, PU/30B-clay nanocomposite films, were prepared using similar procedures while neat PU films were prepared by direct solution casting without adding clay. All samples were stored in an ambient environment for at least 120 h before characterization to ensure that they had reached a near-equilibrium state. The resulting films have a thickness in the range of 0.1 to 0.2 mm.

**Characterization.** The clay loadings in the nanocomposites were determined by thermo-gravimetric analysis (TGA) using TA Instrument TGA Q500. The specimens were heated from 25 °C to 850 °C at 10 °C/min in air with a purge rate of 60 mL/min. On the basis of the TGA results (Supporting Information Figure S1), the nanocomposite samples are named PU/D-clay-0.5%, PU/D-clay-2.8%, PU/D-clay-7.7%, and PU/30B-clay-3.0%, respectively, where the percentages indicate the clay loadings by weight. Their structures and morphologies were characterized using wide-angle X-ray diffraction (WAXD) and transmission electron microscopy (TEM). The films were scanned at room temperature from $2\theta$ = 2° to 40° at a scanning rate of 1°/min using a PANalytical X'Pert PRO diffractometer with Cu $K\alpha$ radiation. In situ high-temperature XRD data was collected on a Siemens D5005 diffractometer equipped with a hot stage. TEM was performed using a JEOL 2100 TEM at 200 kV. The samples were embedded in cured epoxy and microtomed using Leica Ultracut UCT into about 50−100 nm thickness at −100 °C. The tensile properties were measured using an Instron 5567 machine according to ASTM D638 type V at a crosshead speed of 50 mm/min with a 500 N load cell. Samples were cut with a dumbbell die (ASTM D638 type V), and five replicates of each material were used for tensile tests. Tensile-mode DMA measurements were performed using a TA Instrument DMA 2980 at a frequency of 1 Hz and heating rate of 4 °C/min from −100 to 100 °C. The maximum tan $\delta$ values were used to determine the glass transition temperatures. The thermal behaviors of the nanocomposites (sample weight ~15 mg) were characterized using differential scanning calorimetry (DSC) performed on a TA Instrument DSC Q10 at a heating rate of 10 °C/min and modulated DSC (MDSC) on a TA Instrument DSC 2920 at a heating rate of 5 °C/min and a modulating amplitude of 0.796 °C over a period of 60 s. To investigate the morphology of hard microdomains, small-angle X-ray scattering (SAXS) analysis was performed using Anton Paar SAXSess (Austria, 40 kV, 50 mA) equipped with a Cu $K\alpha$ radiation ($\lambda$ = 0.1542 nm) source and an image plate detector at room temperature. All SAXS patterns were collected in transmission mode using the line collimation. The scattering signals were corrected for dark current, background scattering, and Porod, followed by normalization for the primary beam intensity and desmeared prior
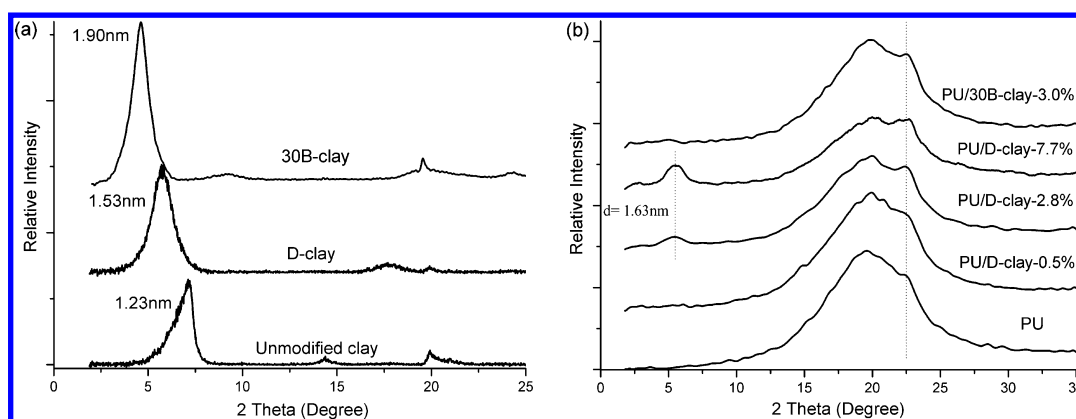
**Figure 1.** WAXD diffraction patterns of (a) pristine clay, D-clay, and 30B-clay and (b) PU/D-clay and PU/30B-clay nanocomposites.
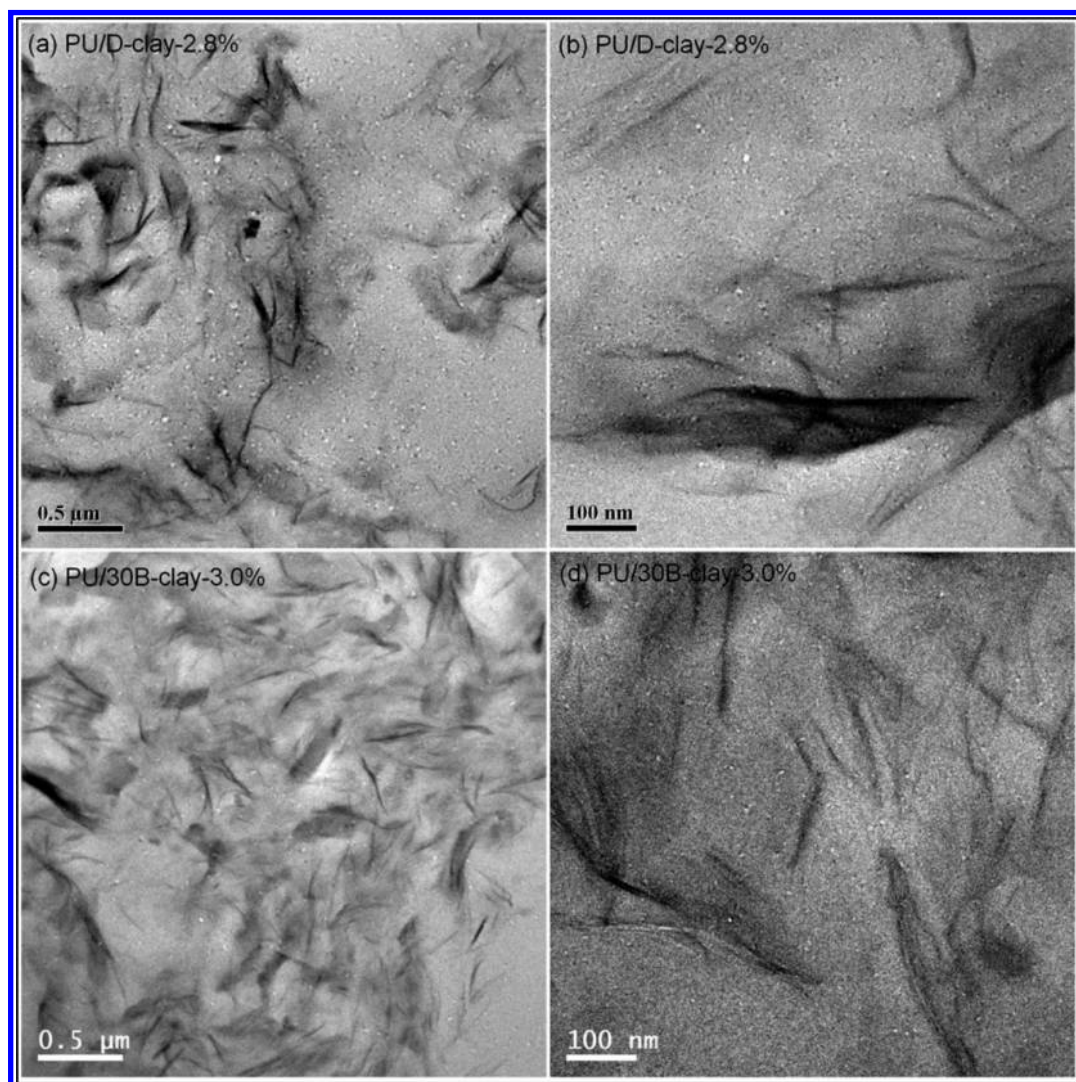


**Figure 2.** Typical TEM images of (a,b) PU/D-clay-2.8% and (c,d) PU/30B-clay-3.0%.

to analysis. FTIR measurements were performed using a Shimadzu FTIR IR Prestige-21 equipped with Golden Gate ATR accessory. Each sample was scanned 32 times at a resolution of 4 cm$^{-1}$, and all the spectra were normalized according to CH$_2$ stretching near 2856 cm$^{-1}$. Deconvolution of the superposed hydrogen-bonded and free carbonyl infrared absorption bands was conducted using the profile fitting program where each band was modeled by a Lorentzian–Gaussian profile function. To calculate the fractions of various type of carbonyl

groups, the areas corresponding to the hydrogen-bonded carbonyl groups were divided by 1.71 to account for the differences in absorptivity between the free and hydrogen-bonded carbonyl groups.[25]

## ■ RESULTS AND DISCUSSION

**Morphology of PU/D-Clay Nanocomposites.** The chemical structures of the PU and clay surface modifiers used
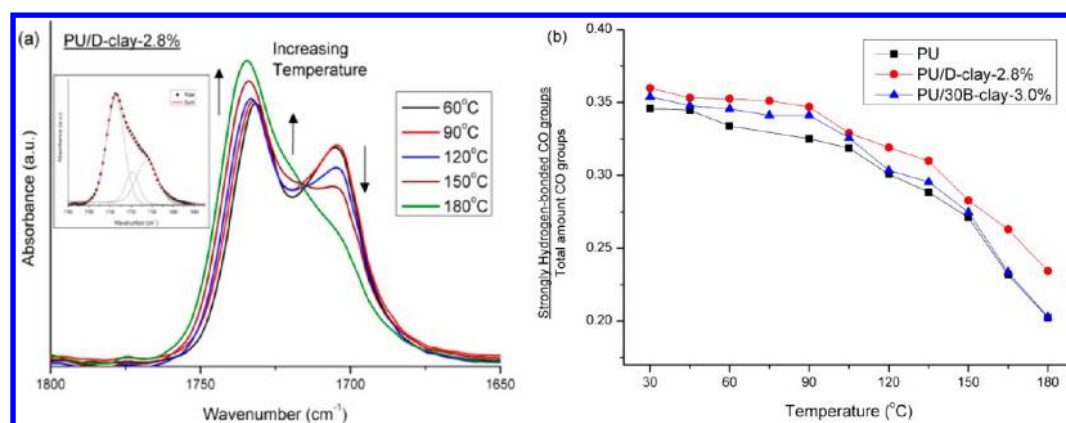
**Figure 3.** (a) FTIR spectra of PU/D-clay-2.8% at different temperatures; the inset shows a typical curve fitting result. (b) Fractions of strongly hydrogen-bonded carbonyl groups of neat PU, PU/30B-clay-3.0%, and PU/D-clay-2.8% (obtained from curve fitting) as a function of temperature.
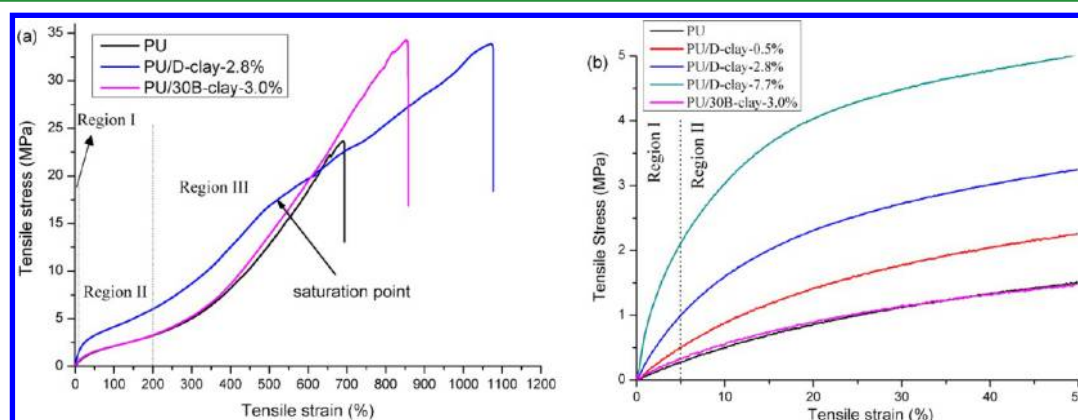


**Figure 4.** (a) Representative tensile stress−strain curves of neat PU and its nanocomposites. (b) The stress−strain curves in Regions I and II showing the variation of the initial modulus and stress of the nanocomposites with clay content.

in this study are shown in Scheme 1. Although both the organic surfactant and PDA are able to form hydrogen bonds with PU, the former contains flexible long alkyl chains whereas the latter has rigid aromatic structure. Furthermore, the catechol groups of PDA can form much stronger hydrogen bonds with PU. The different chemical structures and hydrogen bonding capability of the two types of clay surfaces lead to their different dispersion states in PU, as can be seen below.

Figure 1a shows the WAXD patterns of pristine clay, D-clay and 30B-clay. D-clay exhibits a basal reflection at $2\theta = 5.77°$, corresponding to a $d$-spacing of 1.53 nm, while the basal $d$-spacing of the pristine clay is about 1.23 nm. This implies that the thickness of the PDA coating is about 0.15 nm on either side. When mixed with the PU in DMF, the PU chains can diffuse into the clay interlayer galleries as they have favorable interactions with the catechol groups on D-clay and hydroxyl groups on 30B-clay through hydrogen bonds. From Figure 1b, the peak observed in the region $2\theta < 10°$ is attributed to the intercalated clay; the high-angle peaks are from the PU, which will be discussed in a later section. For all PU/D-clay nanocomposites, a broad peak appears at $2\theta = 5.46°$, implying the presence of intercalated D-clay stacks and probably also a small amount of unintercalated D-clay stacks. With increasing clay loading, the peak becomes more intense but is still broad. In contrast, PU/30B-clay-3.0% does not show any obvious peak in this region, indicating that 30B-clay is better exfoliated in the PU than D-clay. This is corroborated by TEM observations. In the TEM images (Figure 2), the dark riotous areas can be

attributed to the exfoliated thin clay layers, whereas thick clay tactoids can also be observed. Since the samples were produced by casting, there is no preferred orientation for both 30B-clay and D-clay. We can see that, at similar clay loadings, the 30B-clay layers are distributed more uniformly in the PU than the D-clay layers. Moreover, although a mixture of intercalated and exfoliated morphologies was observed for both, 30B-clay is exfoliated to a greater extent than D-clay. The likely reason is that the weak van der Waals forces between the silicate layers of 30B-clay make them easier exfoliated. In contrast, D-clay layers are difficult to be well dispersed, owing to the stronger interactions between the D-clay layers.

The FTIR spectra of PU/D-clay-2.8% at different temperatures are shown in Figure 3a, and the corresponding spectra of PU and PU/30B-clay-3.0% are also given in Supporting Information (cf. Figure S2). Curve fitting for the carbonyl stretching region ($1650-1780$ cm$^{-1}$) was performed in a manner similar to that reported by Runt's group.[27,28] The three bands obtained at $\sim$1704, $\sim$1715, and $\sim$1734 cm$^{-1}$ are attributed to the stretching of strongly hydrogen-bonded, loosely hydrogen-bonded, and free carbonyl groups, respectively, and the fraction of each type of carbonyl groups is obtained by dividing the area of each band by the total area. The results show that PU/D-clay-2.8% has slightly more strongly hydrogen-bonded carbonyl groups than neat PU and PU/30B-clay-3.0% (Figure 3b). More importantly, above 150 °C, the fractions of strongly hydrogen-bonded carbonyl groups of PU and PU/30B-clay reduce more drastically than that of

**Table 1. Tensile Properties of the Neat PU and Nanocomposites**

| sample | initial Young's modulus, $E^a$ (MPa) | $E/E_n{}^b$ (%) | stress at 100% strain (MPa) | tensile strength (MPa) | ultimate elongation (%) |
|---|---|---|---|---|---|
| PU | 5.6 ± 0.4 | | 2.3 ± 0.1 | 24.6 ± 8.3 | 712 ± 148 |
| PU/D-clay-0.5% | 9.6 ± 0.5 | 171 | 2.9 ± 0.1 | 27.7 ± 1.3 | 709 ± 45 |
| PU/D-clay-2.8% | 19.7 ± 0.7 | 352 | 4.0 ± 0.1 | 35.0 ± 1.9 | 1020 ± 128 |
| PU/D-clay-7.7% | 42.1 ± 2.3 | 752 | 5.9 ± 0.2 | 25.3 ± 3.1 | 610 ± 96 |
| PU/30B-clay-3.0% | 6.0 ± 0.3 | 107 | 2.1 ± 0.1 | 33.3 ± 3.1 | 804 ± 78 |

$^a E$ is defined as the stress at 5% strain divided by the strain. $^b E_n$ is the initial modulus of the neat PU.
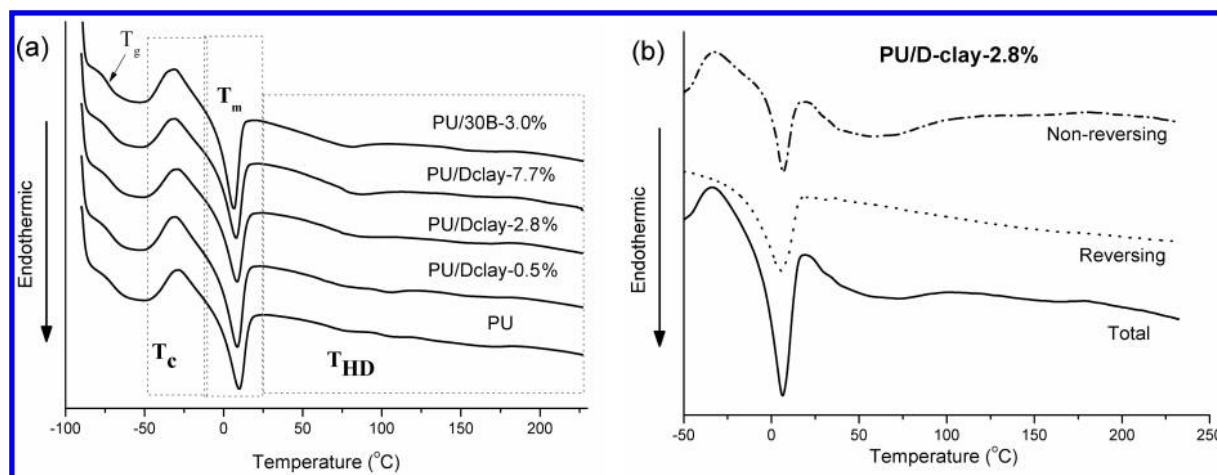


**Figure 5.** (a) Typical DSC first heating curves of neat PU and its nanocomposites. (b) Typical MDSC first heating curves of PU/D-clay-2.8%. In both (a) and (b), the curves have been shifted vertically for clarity.

PU/D-clay-2.8%, owing to the melting of the PU hard domains. This indicates that a large amount of "strongly hydrogen-bonded carbonyl groups" in PU/D-clay-2.8% are hydrogen-bonded to the catechol groups, leading to more stable hydrogen-bonds at high temperatures. The results thus suggest that, although D-clay has less surface area to interact with PU chains than 30B-clay owing to the poorer exfoliation of D-clay, it has stronger tendency to interact with the hard segments than 30B-clay.

**Tensile Properties of PU/D-Clay Nanocomposites.** The tensile stress−strain curves of neat PU and its nanocomposites can be divided into three regions which are clearly marked in Figure 4a. Region I is a quasi-linear region, and the initial modulus measured from this region is governed by the PU crystallinity and tilting of the hard microdomains in the stretching direction.[29] Further increasing the strain will lead to permanent destruction of the hard microdomains; the large hard microdomains will break into smaller ones, and this is followed by two distinct regions of plastic deformation.[29] Herein, we assume 5% strain as the point where the hard microdomains start to break down (that is, the starting point of Region II). In Region II, the slopes of the stress−strain curves initially reduce as the strain increases, owing to the increasing breakdown of the hard microdomains, and then stabilize at a moderate value (Figure 4b), beyond which further plastic deformation in this region is mainly due to the disentanglement of soft microdomains and reorientation of small hard microdomains.[18,29] Region III starts at roughly 200% strain, which is characterized by a steep upturn in the stress−strain curve that is closely related to the strain-induced crystallization of the soft segments[30] until fracture occurs on reaching the tensile strength.

The tensile properties of neat PU and its nanocomposites are summarized in Table 1. Although the dispersion of D-clay in

the PU matrix is slightly poorer than that of 30B-clay, it is striking to see that PU/D-clay-2.8% exhibits not only much higher initial modulus in Region I but also much higher stress in Region II and even larger ultimate elongation than PU/30B-3.0%. By incorporating 2.8 wt % (about 1.2 vol %) of clay into the PU, the initial modulus of PU/D-clay is increased by more than 250% over that of neat PU, whereas PU/30B-clay-3.0% only shows ∼7% increase.

The prominent increase of the initial modulus ($E$) with D-clay could be attributed primarily to the effective load transfer offered by the PDA interface. Given that the catechol groups on the surfaces of D-clay are able to form stronger hydrogen bonds with the hard segments, the stress transfer during stretching is anticipated to be much more effective compared to that with 30B-clay. Furthermore, typical sizes of the hard microdomains vary between 3 and 11 nm,[18] whereas the diameters of D-clay stacks are at submicrometer level. Thus, the tilting of the hard microdomains during stretching also involves rotation of the much larger D-clay stacks, which may also contribute to the much higher modulus obtained. From Figure 4, we can also see that the stress of the PU/D-clay nanocomposites in Region II increases with clay loading, and all values are much higher than those of neat PU and PU/30B-clay nanocomposite. This indicates that a higher stress is required to fracture the hard microdomains, implying that the interactions between the D-clay and the hard segments make the hard microdomains larger and/or stronger. Although 30B-clay can also form hydrogen bonds with the hard segments, the number of available sites is probably fewer as a considerable amount of 30B-clay layers are dispersed in the soft microdomains, as mentioned earlier. Hence, 30B-clay does not increase the initial modulus and Region II stress significantly. In Region III, soft segments crystallize and, hence, a larger stress is required to deform the samples. All PU/D-clay nanocomposites exhibit a saturation

point where the slopes of the tensile stress−strain curves start to decrease (Figure 4 and Supporting Information Figure S3). At this point, the oxygen atoms in the disentangled polyol probably adhere to available hydrogen bonding sites on D-clay and become immobilized, thus hindering the strain-induced crystallization of the soft segments. The higher ultimate elongation of PU/D-clay-2.8% composite may also be a result of the weakened strain-induced crystallization, which leads to improved ductility.

**Effects of D-Clay on PU Crystallization.** To verify that the hard microdomains in the PU/D-clay nanocomposites are indeed stronger and higher in content, the thermal transition behaviors of the as-cast films were characterized using DSC and MDSC. Thermal transitions of TPUs are complicated because they involve multiple processes, including glass transition ($T_g$), crystallization/recrystallization of the soft segments ($T_c$), and their subsequent melting ($T_m$), as well as melting of hard microdomain crystallites of variable sizes ($T_{HD}$).[31] Figure 5a shows the first heating curves of the samples. Above $T_g$, all samples show an exothermic peak followed by an endothermic peak, which can be attributed to the crystallization and melting of soft segment crystallites, respectively. The enhancement in tensile properties is obviously not due to the soft segment crystallization since the melting point of the soft segment is much lower than the mechanical testing temperature (Table 2).

**Table 2. Crystallization and Melting Properties of Neat PU and Its Nanocomposites Measured from Their First Heating DSC Curves**

| sample | $T_g$ (°C) | $T_c$ (°C) | $\Delta H_c$ (J/g) | $T_m$ (°C) | $\Delta H_m$ (J/g) | $\Delta H_{HD}^{NR}$ (J/g) |
|---|---|---|---|---|---|---|
| PU | −72.4 | −27.2 | 11.6 | 6.4 | 15.2 | 14.9 |
| PU/D-clay-0.5% | −72.1 | −29.5 | 13.1 | 6.7 | 17.2 | 18.7 |
| PU/D-clay-2.8% | −72.2 | −28.8 | 11.3 | 6.6 | 15.2 | 21.8 |
| PU/D-clay-7.7% | −72.4 | −29.0 | 10.8 | 7.6 | 16.2 | 26.0 |
| PU/30B-clay-3.0% | −71.9 | −30.4 | 13.1 | 6.2 | 17.1 | 16.3 |

There is no sharp melting endotherm of hard microdomains observed from the DSC curves; hence, it is reasonable to deduce that the hard segment content is fairly low and they are poorly organized. However, there are some broad endotherms above 25 °C for all samples. Since they do not look like typical melting peaks, MDSC was used to probe the nature of these broad endotherms. The reversing heat flow of all samples displays a straight line between 25 and 225 °C, while the nonreversing curve shows a broad endothermic dip between 25 and 180 °C (Figure 5b; also cf. Supporting Information Figure S4). This indicates that the formation of the hard microdomains with random dimensions is a kinetics-controlled process.[31] Indeed, such endotherms can be observed on the second heating curves if the samples are given enough time to recover at room temperature (cf. Supporting Information Figure S5). It is intriguing to note that the hard domain crystallinity estimated from the area of this broad endotherm increases with increasing D-clay loading, suggesting that the strong interfacial interactions between the hard segments and the D-clay promote the time-dependent densification of para-crystalline hard microdomains. SAXS analysis also shows that the addition of D-clay indeed leads to more distinct polymer phase separation (cf. Supporting Information Figure S6).

The presence of para-crystalline hard microdomains is also evidenced by the WAXD data. As mentioned, in Figure 1b, the high angle peaks, including the amorphous halo at around $2\theta = 20°$, are from the PU. As the temperature increases, the amorphous halo becomes broader and shifts toward the low angle side, owing to the increased average interchain distance (Figure 6). For all samples, there is also a shoulder peak at $2\theta = 22.5°$, which is due to the crystallization of the hard segments of PU.[32] It is interesting that the shoulder peak intensity increases with increasing D-clay loading (Figure 1b). This again verifies that the D-clay facilitates the ordering of the para-crystalline hard microdomains. Furthermore, for the PU/Dclay-2.8%, the shoulder peak at about $2\theta = 22.5°$ remains nearly intact up to 115 °C, whereas for the PU/30B-3.0% composite, the shoulder peak almost disappears at 115 °C. This confirms that this peak indeed corresponds to the hard segment crystallites. The strong hydrogen bonding between D-clay and hard segments enables the hard segment crystallites to sustain a higher temperature.

**Dynamic Thermo-Mechanical Properties.** Representative DMA curves of neat PU and its nanocomposites are shown in Figure 7. The corresponding thermo-mechanical property data are listed in Table 3. All the storage modulus ($E'$) curves show a typical glass transition below −40 °C. The $T_g$ values are almost independent of clay loading. Above $T_g$, however, a broad peak is observed on the storage modulus curves roughly between −30 and 10 °C for all specimens, owing to the
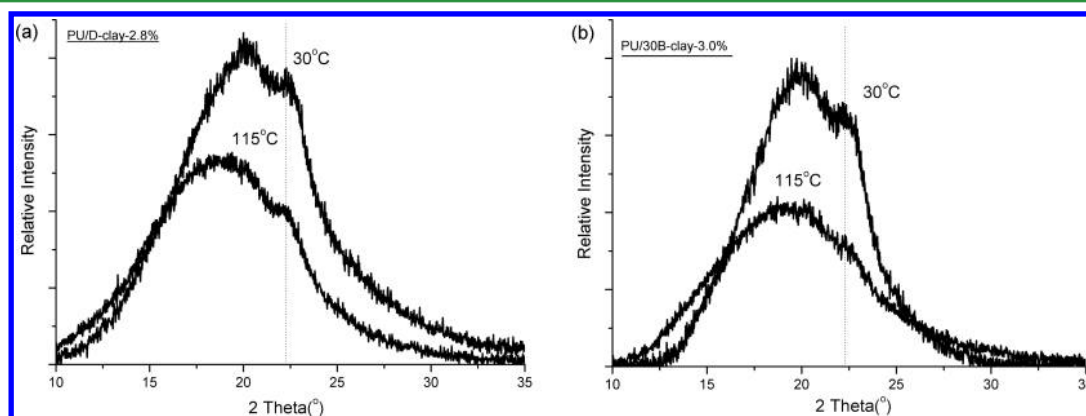


**Figure 6.** WAXD patterns of (a) PU/Dclay-2.8% and (b) PU/30B-3.0% at 30 and 115 °C, showing the effect of temperature on the hard segment crystallites.
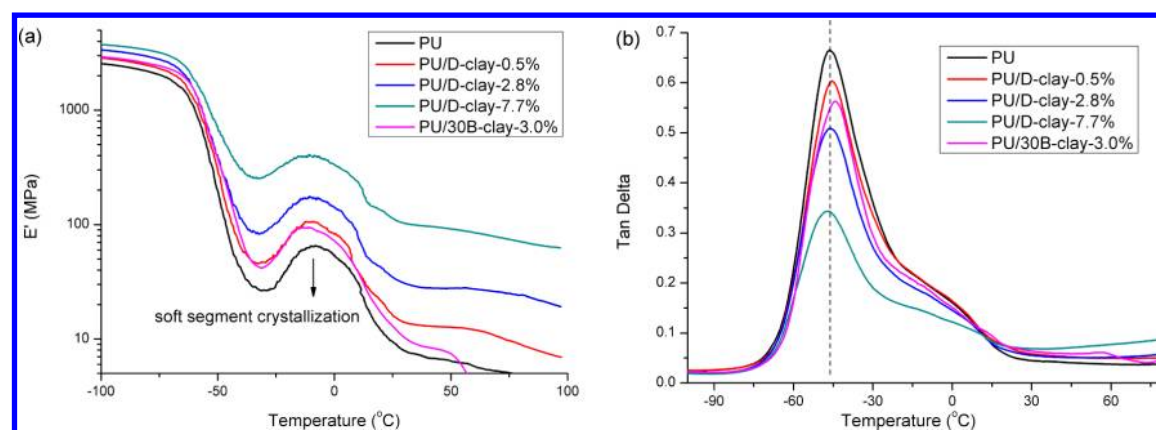
**Figure 7.** Typical (a) storage modulus ($E'$) and (b) tan $\delta$ vs temperature curves of neat PU and its nanocomposites.

**Table 3. Dynamic Thermo-Mechanical Properties of the Neat PU and Nanocomposites**

| sample | peak of tan $\delta$ (°C) | $E'$ @ −80 °C (MPa) | $E'$ @ 25 °C (MPa) | $E'$ @ 50 °C (MPa) | $E'$ @ 100 °C (MPa) |
|---|---|---|---|---|---|
| PU | −46.7 | 2375 | 9.5 | 6.4 | 1.4 |
| PU/D-clay-0.5% | −45.8 | 2465 | 17.5 | 12.7 | 7.0 |
| PU/D-clay-2.8% | −46.5 | 2951 | 34.7 | 27.8 | 19.2 |
| PU/D-clay-7.7% | −46.9 | 3617 | 113.4 | 91.6 | 62.7 |
| PU/30B-clay-3.0% | −43.9 | 2562 | 13.0 | 7.6 | 1.6 |

crystallization and subsequent melting of the soft domains. Upon melting of the soft domains, the hard domains and clays are mainly responsible for the storage modulus. Thus, the storage modulus increases significantly with increasing D-clay loading. The enhancement brought by D-clay is more pronounced than 30B-clay at similar clay loading. With ~3 wt % clay, the improvements imposed by D-clay are three and twelve times higher than those imposed by 30B-clay at 25 and 100 °C, respectively. The storage moduli of all samples exhibit more intense depression above 60 °C (Figure 7a), owing to the melting of the hard microdomains, which is consistent with the DSC results. Nevertheless, with D-clay, the nanocomposite films still exhibit substantial $E'$ values up to 100 °C, which is due to their more stable hard domains as verified by the WAXD results. Hence, D-clay benefits the stiffness at high temperatures.

**Proposed Mechanisms for the Reinforcement Effects.** Scheme 2 illustrates the proposed mechanism for the significantly different reinforcement effects of D-clay and 30B-clay. Without clay, phase separation in the PU is minimal, owing to the low content of the hard segments. With the addition of 30B-clay in PU, the hydroxyl groups on the surfaces of some 30B-clay layers may interact with the hard segments to enhance the initial modulus. However, the attachment of the hard segments on 30B-clay, which has flexible long alkyl chains, also enhances the dissolution of the hard segments into the soft microdomains. Hence, there are some hard segments and clay layers dispersed in the soft segment matrix. In contrast, D-clay is more compatible and interacts strongly with the hard segments; this not only leads to more hydrogen bonds between hard segments and D-clay stacks but also induces further phase separation and densification of the poorly organized hard microdomains. Consequently, the hard microdomains are more difficult to be stretched, tilted, and broken down, leading to

**Scheme 2. Schematic Illustration of Phase Separation in (a) Neat PU, (b) PU/30B-Clay, and (c) PU/D-Clay Nanocomposites[a]**
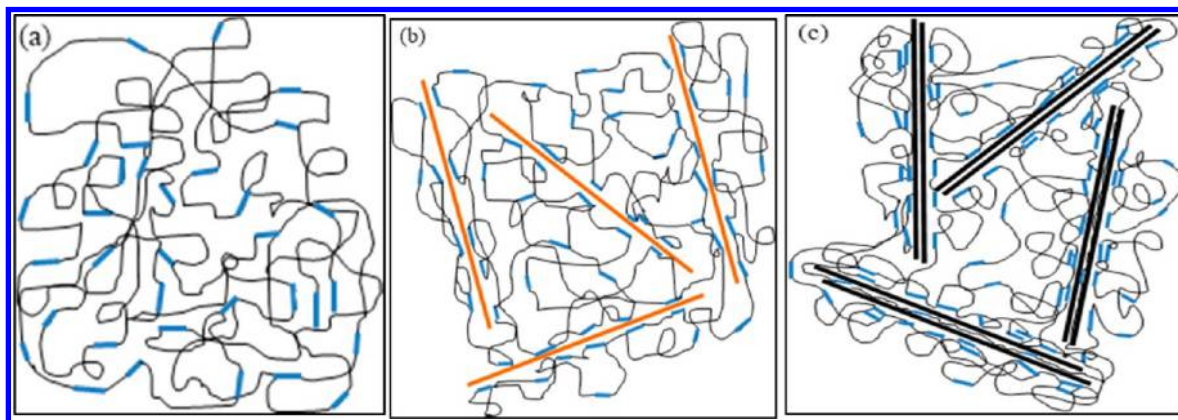


[a]The black, thin line represents soft segment; the blue, thick line represents hard segment; the orange, thick line represents 30B-clay; the black, thick line represents D-clay. The diagrams are not drawn to scale.

much higher initial modulus and Region II stress without sacrificing the elasticity.

## CONCLUSIONS

In summary, we reported a facile method to enhance interfacial interaction between clay and PU matrix. Nearly a monolayer of PDA was coated on the clay surface, and D-clay was dispersed in the PU matrix by solvent blending. The strong hydrogen bonding interaction between the hard segments of PU and D-clay encourages more ordered packing of the hard segments, promoting polymer phase separation. The stable hard micro-domains in the vicinity of D-clay hinder the movement of polymer chains, resulting in substantial improvements in mechanical properties, including initial modulus, tensile strength, and elongation at break, at a very low clay loading. The presence of strong hydrogen bonds also increases the stiffness of the PU at high temperatures, making the PU/D-clay nanocomposites a good candidate for high temperature applications.

## ASSOCIATED CONTENT

### Ⓢ Supporting Information

TGA results of PU and PU/clay nanocomposites; FTIR spectra of PU and PU/30B-clay-3.0% at different temperatures; representative tensile stress−strain curves of PU/D-clay nanocomposites; MDSC data of PU and PU/clay nano-composites; DSC curves of neat PU recorded at different times after quenching; SAXS profiles of PU and PU/clay nanocomposites. This material is available free of charge via the Internet at http://pubs.acs.org.

## AUTHOR INFORMATION

### Corresponding Author
*E-mail: asxhlu@ntu.edu.sg.

### Notes
The authors declare no competing financial interest.

## ACKNOWLEDGMENTS

## REFERENCES

(1) Podsiadlo, P.; Kaushik, A. K.; Arruda, E. M.; Waas, A. M.; Shim, B. S.; Xu, J.; Nandivada, H.; Pumplin, B. G.; Lahann, J.; Ramamoorthy, A.; Kotov, N. A. *Science* **2007**, *318*, 80−83.
(2) Zhao, H.; Robertson, N. B.; Jewhurst, S. A.; Waite, J. H. *J. Biol. Chem.* **2006**, *281*, 11090−11096.
(3) Waite, J. H. *Nat. Mater.* **2008**, *7*, 8−9.
(4) Lee, H.; Scherer, N. F.; Messersmith, P. B. *Proc. Natl. Acad. Sci. U. S. A.* **2006**, *103*, 12999−13003.
(5) Zhou, W. H.; Lu, C. H.; Guo, X. C.; Chen, F. R.; Yang, H. H.; Wang, X. R. *J. Mater. Chem.* **2010**, *20*, 880−883.
(6) Yang, L.; Kong, J.; Yee, W. A.; Liu, W.; Phua, S. L.; Toh, C. L.; Huang, S.; Lu, X. *Nanoscale* **2012**, *4*, 4968−4971.
(7) Yang, L.; Yee, W. A.; Phua, S. L.; Kong, J.; Ding, H.; Cheah, J. W.; Lu, X. *RSC Adv.* **2012**, *2*, 2208−2210.
(8) Lee, H.; Dellatore, S. M.; Miller, W. M.; Messersmith, P. B. *Science* **2007**, *318*, 426−430.
(9) Podsiadlo, P.; Liu, Z.; Paterson, D.; Messersmith, P. B.; Kotov, N. A. *Adv. Mater.* **2007**, *19*, 949−955.
(10) Kaushik, A. K.; Podsiadlo, P.; Charles, M. Q.; Shaw, M.; Waas, A. M.; Kotov, N. A.; Arruda, E. M. *Macromolecules* **2009**, *42*, 6588−6595.
(11) Bonderer, L. J.; Studart, A. R.; Gauckler, L. J. *Science* **2008**, *319*, 1069−1073.
(12) Pei, A.; Malho, J. M.; Ruokolainen, J.; Zhou, Q.; Berglund, L. A. *Macromolecules* **2011**, *44*, 4422−4427.
(13) Khan, U.; May, P.; O'Neill, A.; Vilatela, J. J.; Windle, A. H.; Coleman, J. N. *Small* **2011**, *7*, 1579−1586.
(14) Maji, P. K.; Guchhait, P. K.; Bhowmick, A. K. *ACS Appl. Mater. Interfaces* **2009**, *1*, 289−300.
(15) Qian, Y.; Lindsay, C. I.; MacOsko, C.; Stein, A. *ACS Appl. Mater. Interfaces* **2011**, *3*, 3709−3717.
(16) Mishra, A.; Purkayastha, B. P. D.; Roy, J. K.; Aswal, V. K.; Maiti, P. *Macromolecules* **2010**, *43*, 9928−9936.
(17) Osman, A. F.; Edwards, G. A.; Schiller, T. L.; Andriani, Y.; Jack, K. S.; Morrow, I. C.; Halley, P. J.; Martin, D. J. *Macromolecules* **2011**, *45*, 198−210.
(18) Liff, S. M.; Kumar, N.; McKinley, G. H. *Nat. Mater.* **2007**, *6*, 76−83.
(19) Chavarria, F.; Paul, D. R. *Polymer* **2006**, *47*, 7760−7773.
(20) Guo, S.; Zhang, C.; Peng, H.; Wang, W.; Liu, T. *Compos. Sci. Technol.* **2011**, *71*, 791−796.
(21) Tien, Y. I.; Wei, K. H. *Macromolecules* **2001**, *34*, 9045−9052.
(22) Chen, T. K.; Tien, Y. I.; Wei, K. H. *Polymer* **2000**, *41*, 1345−1353.
(23) Chen-Yang, Y. W.; Lee, Y. K.; Chen, Y. T.; Wu, J. C. *Polymer* **2007**, *48*, 2969−2979.
(24) Yang, L.; Phua, S. L.; Teo, J. K. H.; Toh, C. L.; Lau, S. K.; Ma, J.; Lu, X. *ACS Appl. Mater. Interfaces* **2011**, *3*, 3026−3032.
(25) Coleman, M. M.; Lee, K. H.; Skrovanek, D. J.; Painter, P. C. *Macromolecules* **1986**, *19*, 2149−2157.
(26) Xu, L. Q.; Yang, W. J.; Neoh, K.-G.; Kang, E.-T.; Fu, G. D. *Macromolecules* **2010**, *43*, 8336−8339.
(27) Hernandez, R.; Weksler, J.; Padsalgikar, A.; Taeyi, C.; Angelo, E.; Lin, J. S.; Xu, L. C.; Siedlecki, C. A.; Runt, J. *Macromolecules* **2008**, *41*, 9767−9776.
(28) Pongkitwitoon, S.; Hernández, R.; Weksler, J.; Padsalgikar, A.; Choi, T.; Runt, J. *Polymer* **2009**, *50*, 6305−6311.
(29) Yeh, F.; Hsiao, B. S.; Sauer, B. B.; Michel, S.; Siesler, H. W. *Macromolecules* **2003**, *36*, 1940−1954.
(30) Finnigan, B.; Jack, K.; Campbell, K.; Halley, P.; Truss, R.; Casey, P.; Cookson, D.; King, S.; Martin, D. *Macromolecules* **2005**, *38*, 7386−7396.
(31) Wang, L. F. *Eur. Polym. J.* **2005**, *41*, 293−301.
(32) Zia, K. M.; Bhatti, I. A.; Barikani, M.; Zuber, M.; Bhatti, H. N. *Carbohydr. Polym.* **2009**, *76*, 183−187.